Atmos. Chem. Phys. Discuss., 9, 20775–20817, 2009
www.atmos-chem-phys-discuss.net/9/20775/2009/

Atmospheric Chemistry and Physics Discussions

This discussion paper is/has been under review for the journal *Atmospheric Chemistry and Physics (ACP)*. Please refer to the corresponding final paper in *ACP* if available.

Turbulence associated with mountain waves over Northern Scandinavia – a case study using the ESRAD VHF radar and the WRF mesoscale model

S. Kirkwood[1], **M. Mihalikova**[1], **T. N. Rao**[2], **and K. Satheesan**[1]

[1]Swedish Institute of Space Physics, Box 812, 98128 Kiruna, Sweden
[2]National Atmospheric Research Laboratory, Gadanki, India

Received: 6 July 2009 – Accepted: 7 September 2009 – Published: 2 October 2009

Correspondence to: S. Kirkwood (sheila.kirkwood@irf.se)

Published by Copernicus Publications on behalf of the European Geosciences Union.

Abstract

We use measurements by the 52 MHz wind-profiling radar ESRAD, situated near Kiruna in Arctic Sweden, and simulations using the Advanced Research and Weather Forecasting model, WRF, to study vertical winds and turbulence in the troposphere in mountain-wave conditions on 23 , 24 and 25 January 2003. We find that WRF can accurately match the vertical wind signatures at the radar site when the spatial resolution for the simulations is 1 km. The horizontal and vertical wavelengths of the dominating mountain-waves are ∼10–20 km and the amplitudes in vertical wind 1–2 m/s. Turbulence below 5500 m height, is seen by ESRAD about 40% of the time. This is a much higher rate than WRF predictions for conditions of Richardson number (R_i) <1 but similar to WRF predictions of R_i<2. WRF predicts that air crossing the 100 km wide model domain centred on ESRAD has a ∼10% chance of encountering convective instabilities (R_i<0) somewhere along the path. The cause of low R_i is a combination of wind-shear at synoptic upper-level fronts and perturbations in static stability due to the mountain-waves. Comparison with radiosondes suggests that WRF underestimates wind-shear and the occurrence of thin layers with very low static stability, so that vertical mixing by turbulence associated with mountain waves may be significantly more than suggested by the model.

1 Introduction

The Scandinavian mountain chain acts as a significant barrier to westerly winds from the North Atlantic (see Fig. 1). Winter storm tracks very often bring deep depressions into the region and strong westerly winds across the mountain chain are a common result. It is well known that strong winds across mountain chains can lead to the formation of mountain lee waves, and these waves have long been recognised over the Scandinavian mountains (e.g. Larsson, 1954). Mountain waves have been particularly well studied over the mountain chains in western USA, where they can lead to ex-

ACPD

9, 20775–20817, 2009

treme turbulence, and more rarely, to aircraft accidents see e.g. (Doyle and Durran, 2002; Doyle and Duran, 2004) and references therein. The Scandinavian mountains are not as high as the mountains of western USA, and there is much less air traffic, so turbulence associated with Scandinavian mountain waves is less important for air-safety. However, turbulence is potentially of substantial interest for its role in mixing atmospheric constituents between different heights.

The stratosphere, and the troposphere in high-latitude regions, such as Scandinavia, are generally considered to be statically stable (except in sporadic summer thunderstorms). Large scale models which trace air-mass transport, for example in considering downward transport of ozone from the stratosphere, generally assume no vertical mixing, or a small fixed diffusion coefficient, in these regions (Stohl et al., 2005). Such models find that ozone from the stratosphere contributes very little to ozone concentrations in the lower troposphere (Sprenger and Wernli, 2003; James et al., 2003; Stohl, 2006), in contrast to chemical tracer studies which suggest a much higher contribution (e.g. Dibb et al., 2003) .

Turbulence due to breaking mountain waves has been recognised as a potential source of vertical mixing (Dörnbrack, 1998), but whether or not this is a significant process on a regional or climatological scale remains to be determined. However, in the context of mixing between the stratosphere and troposphere, it is worth noting that tropopause folds, which bring stratospheric air to low altitudes through isentropic transport, often pass over the Scandinavian mountains (Rao et al., 2008). These are often associated with high-speed westerly winds at the surface, which will lead to mountain waves with the potential for associated turbulence (Rao and Kirkwood, 2005). There is a significant seasonal variation in the occurrence of folds, with a winter maximum (Rao et al., 2008), which is a potential contributing factor to the seasonal variation of ozone in the free troposphere (Rao et al., 2003). There is also an unexplained seasonal variation in surface ozone in the polar regions, with observed wintertime concentrations substantially higher than the values predicted by state-of-the-art models (Tarasova et al., 2007; Zeng et al., 2008). Vertical mixing in association with the winter

maximum in tropopause folds might explain this feature, if the mixing is strong enough.

The best available observational method for direct observations of atmospheric turbulence with climatological time coverage is atmospheric radar (see e.g. Wilson, 2004 for a review). Radar observations give a direct estimate of the root mean square (r.m.s) turbulent velocities (in the vertical direction) in air parcels passing overhead of the radar site, and of their temporal variability at that single location. Multi-year statistics of the amount and occurrence rates of turbulence have been published for a number of locations, in the USA, Japan and India (Nastrom et al., 1986; Fukao et al., 1994; Kurosaki et al., 1996; Nastrom and Eaton, 1997, 2005; Rao et al., 2001). Translating this information to quantitative estimates of vertical mixing on a regional scale requires knowledge of both the processes causing the turbulence and of the spatial and temporal variability of the turbulence. The studies mentioned above have considered the relationship between turbulence and synoptic weather conditions, but not the relationship to mountain waves, although a statistical correlation between enhanced turbulence and gravity waves was noted by Nastrom et al. (1986).

The ESRAD (ESrange RADar) VHF wind-profiling radar (Chilson et al., 1999) has been in essentially continuous operation since late 1996. This radar is situated on the lee side of the Scandinavian mountain chain at 67.9° N, 21.1° E (see Fig. 1), and often sees the signatures of mountain waves (Réchou et al., 1999). Our aim in this study is to determine whether, with the help of a mesoscale atmospheric model, we can understand the conditions leading to the turbulence which is often seen by the radar in association with mountain waves. This is an essential first step to be able to use radar turbulence observations to help quantify the amount of turbulent mixing taking place on a regional and climatological scale.

A number of studies in the last decade have discussed mountain lee waves generated by the Scandinavian mountain chain, on the basis of 3-D models. However, most of these have focussed on the propagation of the lee-waves to the stratosphere, and the resultant effects on polar stratospheric clouds or on momentum transfer to the middle-atmosphere circulation (e.g. Dörnbrack et al., 2002; Serafimovich et al.,

2006). Those studies have used model grids with horizontal resolution of 10s of kilometres, so that only waves with very long horizontal wavelengths (100 s of km) were resolved. The vertical wind fluctuations associated with these waves are small, a few cm/s, and wave-related turbulence in the troposphere or lower stratosphere has not been an issue. However, it is easily recognised in observed cloud patterns that high-amplitude mountain waves with much shorter wavelengths are commonplace in both the troposphere and the stratosphere. Recent developments in mesoscale modelling and computing power have led to a number of 3-D modelling studies at more appropriate horizontal resolution. For example, Doyle et al. (2005), observed and modelled (using 1.7 km horizontal resolution) breaking mountain waves over Greenland. They found evidence for amplitudes in vertical winds of 1–5 m/s and turbulence associated with wave breaking in both the troposphere and stratosphere. In situ observations by research aircraft and dropsondes provided validation, at least of the general characteristics of the wave disturbances. Maturilli and Dörnbrack (2006), modelled waves over Svalbard (with 4 km horizontal resolution) and found waves with 10–20 km horizontal wavelength, and amplitude up to a few m/s in vertical wind. Only indirect validation of the model results was possible in terms of observation (by lidar) of polar stratospheric clouds composed of ice. It was also pointed out that this was a unique event in 15 years of lidar observations from that site. Pluogonven et al. (2008), modelled mountain waves over the Antarctic peninsula (using a 7 km horizontal resolution). They found horizontal wavelengths 65–80 km and a few m/s amplitude in vertical winds. The model supported the conclusion that turbulence in the lower stratosphere was responsible for the loss of a long-duration balloon as it crossed the area. Oscillations in the float height of second balloon passing nearby provided a reasonable validation of the horizontal wavelength and vertical wind amplitude. Generally, for these cases, possibilities to validate the model simulations were limited and there is no way to assess how representative such events are for the locations where they were observed (rather the opposite – the events were studied because of their uniqueness).

In this study we will look at a typical, rather than a unique event. We will use the Ad-

vanced Research Weather Research and Forecasting model (WRF-ARW Skamarock et al., 2005, 2007), which has already been applied with considerable success to modelling mountain waves at high-latitudes (Pluogonven et al., 2008), and we will use radiosondes and atmospheric radar measurements for more comprehensive validation than has previously been attempted. For our case-study we have chosen the period 23–25 January 2003 since, during this period, an unusually high number of radiosondes were launched from Esrange as part of the MaCWAVE campaign (Goldberg et al., 2006). The mountain wave characteristics are typical for this radar site – similar wave amplitudes and turbulent velocities are seen 40 % of the time during the winter months September to April. We will focus on the troposphere, in particular the lower troposphere, since these are the heights where the radar detects unexpected turbulence. A synoptic overview of the period is given in the next section. Previously published studies from this campaign also describe the meteorological situation over a longer period (Blum et al., 2006) and comparative observational and modelling results for inertial gravity waves, including their propagation to mesospheric heights, can be found in Wang et al. (2006); Serafimovich et al. (2006); Hoffmann et al. (2006).

2 Synoptic overview

The synoptic situation is described on the basis of analysis of surface and upper-air charts as given in the European Meteorological Bulletin (http://dwd-shop.de/gb/0095.en.htm) for the days 23 to 25 January 2003 and as shown by the European Centre for Medium Range Weather Forecasting (ECMWF) reanalysis for the same time-frame.

On 23 January 2003, a deep depression was centered over the Svalbard archipelago (to the north of the Scandinavian Peninsula). On its rear side south-westerly to westerly winds with velocities of 25 to 35 m/s around the 300 hPa level and 20 to 30 m/s between the 700 and 500 hPa levels were observed over the Scandinavian Mountain Range. In the lower troposphere (850 hPa level) the wind velocities reached around 15 m/s. Between this depression and a ridge of high pressure that extended from the

southwest to the Scandinavian Peninsula a westerly jet stream (wind velocities of 45 to 55 m/s) was detected around the 300 hPa level on 24 of January 2003. Wind velocities have also increased at the lower levels of the troposphere to 25–35 m/s between 700 and 500 hPa (Fig. 2), and up to 25 m/s at 850 hPa. In the evening the wind velocities temporarily dropped down. The low pressure system was moving slowly towards the southeast. West of the Scandinavian Peninsula a trough of low pressure started to form and, on 25 January, it caused a change of wind direction over the northern part of the Scandinavian mountain range to northwesterly, which is perpendicular to the mountains (Fig. 2). At this time (early morning of 25 January) waves could be observed in the cloud structure on the NOAA satellite image (Fig. 3) on the lee side of the Scandinavian Mountain Range. Wind velocities remained above 40 m/s around 300 hPa and 15 to 25 m/s between 850 and 500 hPa for the most part of the day.

3 Radiosonde observations

Altogether 8 GPS radiosondes were launched on 23 and 24 January 2003 as part of the MaCWAVE sounding rocket campaign (Goldberg et al., 2006). Here we use cleaned data sampled at 10 s (~50 m) resolution. Profiles of wind speed and static stability, in terms of buoyancy frequency, ω_B, are shown by the blue lines in Fig. 4. Note that no wind measurements were available from the first sonde.

4 ESRAD observations

ESRAD is an interferometric VHF radar operating at 52.5 MHz. It is located at Esrange (Kiruna, Sweden, 67.9° N, 21.1° E) and has been operating essentially continuously since August 1996 (Chilson et al., 1999). The measurements used here are height profiles of signal strength, of vertical winds determined from the Doppler shift of the returned signal, and of horizontal winds and r.m.s. velocity fluctuations determined by

the full correlation (f.c.a.) technique (Briggs, 1984; Holdsworth et al., 2001; Holdsworth and Reid, 2004). The height resolution of the measurements on this occasion was 300 m, and each profile represents an average over 51 seconds, with measurements repeated each 2 min. The radar antenna (at the time of this case study) consisted of 140 yagi-antennas, arranged in a 12×12 square array (with 4 antennas missing in the centre). For echo power and vertical wind estimates, the whole antenna was used, corresponding to a beam width of ∼6° (full width, half maximum). For f.c.a. measurements, the whole array was used for transmission, but the array was divided into 6 rectangular sub-arrays, each of 4×6 antennas, for reception. Each f.c.a. measurement-point in a height profile corresponds to an average over a cylinder which is 300 m thick in the vertical direction and has a diameter which varies from ∼180 m at 2000 m height to 900 m at 10 000 m height, vertically above the radar.

In principle, the height profile of radar echo power returned from the troposphere and lower stratosphere should depend on the distance from which the echo is returned, atmospheric density, static stability, humidity gradients and the fine-scale structure of temperature and density fluctuations within the scattering volume (e.g. Gage, 1990). In practice, for vertically pointing radars operating around 50 MHz, the first three parameters have been found to dominate and echo power can be scaled to provide an estimate of static stability

$$R_B^2 = F_e z \exp(-z/H) P_r^{1/2} \quad (1)$$

where P_r is radar echo power, z is height (also distance from the radar), H is the atmospheric scale height (so $\exp(-z/H)$ gives the height variation of atmospheric density), $R_B = \omega_B$, the atmospheric buoyancy frequency, in the upper troposphere and lower stratosphere (where humidity is negligible). F_e has been found to be independent of height and time at least over heights from 5000–20 000 m in the upper troposphere/lower stratosphere and over the several hours duration of the experiments so far reported (Hooper et al., 2004; Luce et al., 2007).

The constant of proportionality F_e can be found using a single radiosonde and a

check on the applicability of the equation is provided by comparing with further radiosondes. The radar-derived R_B are shown by the black lines in Fig. 4 (upper panel), where the first sonde has been used to determine F_e. The vertical resolution of the sonde measurements is about 50 m, and the radar estimates have been averaged for 30 min following the sonde launch. The agreement between the radar-derived R_B and the sonde-derived ω_B is good, bearing in mind that the sondes do not sample exactly the same volume as the radar – by the time they reach the tropopause at ~8000 m they are typically ~40 km downwind. There is more detail in the vertical profiles measured by the sondes which is understandable since the radar averages over a nominal 300 m height interval (in practice a Gaussian-weighted height interval with a 300 m width at half power). In addition, the radar estimate does not capture the very low values of ω_B sometimes found by the sondes in the upper troposphere (14, 16, 19 and 22:00 UTC on 24 January), and on a few occasions in the lower troposphere (12 and 14:00 UTC on 23 January). The complete time-height series of R_B calculated from the radar echo power is shown in the top panel of Fig. 5. The most conspicuous feature is the tropopause, marked by a rapid increase of R_B at heights varying between 5000 and 10 000 km. Warm fronts, marked by narrow layers of enhanced R_B, can be seen descending from the tropopause early on 24 January and early on 25 January. The high values of R_B throughout the upper troposphere (above 5000 m) on the afternoon of 23 January, with no distinct tropopause (see also the first two radiosonde profiles in Fig. 4) , correspond to an equatorward extension of the deep depression centred further north, which is described in the synoptic overview.

The second and third panels (from the top) of Fig. 5 show the horizontal wind-speed and direction, determined by the f.c.a. technique. This technique assumes that a time-varying ensemble of scatterering structures (which may be anisotropic), are responsible for the radar echo. The signal scattered from these structures leads to a diffraction pattern on the ground, moving horizontally at twice the horizontal drift speed of the scatterers and changing over time. With an assumption that the temporal and spatial correlation functions of the diffraction pattern can be described by the same functional

form (usually assumed to be gaussian), the temporal and (horizontally anisotropic) spatial correlation scales, and the horizontal drift speed can be determined from the auto- and cross-correlations of the signals received on at least three non-colinear receiving antennas. The resulting drift speed is usually called the true wind. In case the assumed conditions are not satisfied, an apparent wind speed can be calculated based only on the time-delay for maximum cross-correlation between antenna pairs. This gives an upper estimate of the wind speed. In the present case-study, 5 receiving sub-arrays were available giving an overdetermined system, so that a least-squared fit was used to determine the best solution for each height and time. Figure 4 (lower panels) compares the f.c.a. wind estimates with radiosonde winds. The agreement is generally good but indicates that the f.c.a. true winds tend to underestimate wind speed at times, particularly in the upper troposphere/ lower stratosphere. In these cases the apparent wind speed is closer to that measured by the radiosonde. (There is no significant difference between the directions of the true, apparent and radiosonde winds.)

The fourth panel of Fig. 5 shows the vertical wind component measured by the radar. This is simply the mean Doppler shift of the echo, expressed in m/s, and with reversed sign so that positive values correspond to upward motion. This is determined using the whole antenna so it corresponds to a rather narrow radar beam (6°). In principle it is possible that these vertical winds might include a small component of horizontal wind, if scattering structures are systematically situated to one side of zenith. For example, a horizontal wind of 20 m/s would give an apparent vertical component of up to 1 m/s if a scatterer from a region 2° off zenith dominates the returned signal. However, when we compare with the model results in the next section, we will see that there is no reason to believe that this is a significant effect. The vertical wind in Fig. 5 is characterised by alternating periods of strong (~1 m/s) upward and downward motion, coherent over vertical distances of 5 km to at least 12 km. The amplitude of the vertical winds is highest on the afternoon of the 23 January and the morning of 25 January , when the horizontal winds at low altitudes are from directions between west and north.

The fifth (bottom) panel of Fig. 5 shows when enhanced levels of turbulence are de-

ACPD
9, 20775–20817, 2009

tected. This is based on the equivalent root mean square velocity spread, V_τ calculated from the diffraction patterns intrinsic correlation time, τ, using the f.c.a. technique.

$$V_\tau = \lambda(2\ln 2)^{1/2}/4\pi\tau \quad (2)$$

where λ is the radar wavelength.

In the case that the scattering volume is filled with turbulent eddies, the latter will have random vertical velocities. Averaging over the scattering volume and over the time of each measurement (51 s) will give $V_\tau = V_{\mathrm{RMS}}$, the r.m.s. random velocity component or, equivalently, the standard deviation of the random vertical motions, provided that this vertical motion is the dominating factor determining the correlation time of the diffraction pattern. As discussed in Holdsworth et al. (2001), the f.c.a. technique, together with an interferometric antenna array such as that available for ESRAD, then gives a direct estimate of V_{RMS}. There is no need for the kind of beam-width / wind-speed corrections which must be applied in the case of non-interferometric Doppler-beam-swinging radars which estimate V_{RMS} from the spectral width of the echoes (see e.g. Cohn, 1995, for a discussion).

However, although V_τ can be calculated for all heights and times, it cannot always be assumed that $V_\tau = V_{\mathrm{RMS}}$. Figure 6 shows height profiles of the median values of the radar signal strength and the diffraction-pattern correlation time τ, for the three days of our case study. This shows two distinct regimes: high power (falling off with distance from the radar) and long correlation times below 5500 m, low power and much shorter correlation times above 5500 m. It is well known that both turbulent eddies (volume scatter) and quasi-specular reflection (fresnel scattering) can contribute to the radar echoes from the lower atmosphere (e.g. Gage, 1990) and it is likely that the two distinct regimes in Fig. 6 correspond to these different mechanisms. We would not expect turbulence to be active at all heights and times, so we can use the median values as an indication of the diffraction-pattern correlation time due to non-turbulent processes, which correspond to $V_\tau \sim 0.2$ m/s in the lower troposphere where the median value of $\tau \sim 2.5$ s and $V_\tau \sim 1$ m/s at the upper heights where the median value of $\tau \sim 0.5$ s.

ACPD
9, 20775–20817, 2009

We can be confident that the radar is detecting the signature of turbulence, and that V_τ is a reasonable estimate of V_{RMS} only when V_τ is significantly higher than these values. So the lowest panel of Fig. 5 shows $V_{RMS} \sim V_\tau > 0.3$ m/s below 5000 m height and $V_{RMS} \sim V_\tau > 2$ m/s above that height.

It is clear from Fig. 5 that high values of V_{RMS} prevail in the lower troposphere below about 4 km height, from midday on 23 January to midday on 25 January, and are most persistent during essentially the same intervals when mountain-wave signatures are strongest in the vertical wind. There are also scattered observations of high V_{RMS} in the upper troposphere on the morning of the 24 January and the afternoon of 25 January, but these are not as persistent as the turbulence at lower heights.

The first two radiosondes in Fig. 4 were launched at times when reasonably strong turbulence was detected by ESRAD, between 2000 and 3000 m height, at 12:00 and 14:00 UTC on 23 January . The next two sondes, at 12:00 and 14:00 UTC on 24 January coincide with enhanced turbulence seen by ESRAD in the upper troposphere. The sondes detected narrow regions with very low values of ω_B in the same height regions as the radar turbulence observations. These would allow not only shear instability but, in some cases, convective instability, consistent with the turbulence observed by the radar.

5 WRF-ARW model simulations

The WRF-ARW model, described by Skamarock et al. (2005, 2007) allows non-hydrostatic simulation of mountain waves based on high-resolution topography. Here we have used WRF version 2.1 with two-way nested domains, as shown in Fig. 1, with horizontal resolutions of 15 km (outermost domain), 3 km (intermediate domain) and 1 km (the innermost domain around the location of ESRAD), respectively. Results from the 1 km domain at the location of ESRAD are illustrated in Fig. 5. For the model runs, conditions at the outer boundary were provided by National Center for Environmental Protection (NCEP) final analyses at 1°, and 6 h resolution. For cloud microphysics, the

ACPD
9, 20775–20817, 2009

3-class simple scheme following Hong and Chen (2004) was used, the 3 classes being vapour, cloud water/ice, rain/snow with ice or snow being assumed when the temperature is below freezing. For longwave radiation the RRTM look-up table scheme was used (Mlawer et al., 1997) and for shortwave radiation the scheme described by Dudhia (1989). No cumulus effects were included. The land surface is treated by a 5-layer surface thermal diffusion scheme (Skamarock et al., 2005, 2007). Runs were made with two different surface layer/boundary layer schemes (MM5-YSU and Eta-MYJ Skamarock et al., 2005, 2007). Both schemes account for heat, moisture and momentum exchange with the surface, but use different models of turbulence in the boundary layer. No significant difference between the results using the two schemes was found for the parameters studied in the present comparison. Runs were made using 50 hPa and 10 hPa top limits, and for several different vertical spacings of the model levels. No significant influence of the top height was found for the height region addressed here, i.e. between 0–13 000 m. The dependence of the results on the vertical resolution is discussed below. The results shown in Fig. 5 are for a model run using 66 model levels between the surface and 50 hPa with the spacing between model levels about 150 m up to 5000 m height, 350 m up to 10 000 m, and 500 m above there. Model runs were also made with 28 and 56 default model levels, which have closer spacing in the boundary layer (up to ~1200 m) and about 700 m or 350 m spacing in the troposphere, respectively. Runs were further made both with, and without, the inner nested grids.

Figure 5 shows the model results in the inner domain (horizontal resolution 1 km), at the location of the ESRAD radar, at 5-minute resolution. The top 4 panels show buoyancy frequency, wind speed, wind direction, and vertical wind, respectively. Comparison with Fig. 5 shows that there is good agreement with the ESRAD measurements although there is more detail in the local observations on short time scales. This is unavoidable given the 6 h resolution of the input meteorological data for the model. Figure 4 provides a comparison of the WRF estimates (in red) of ω_B and of wind, with the radiosondes (blue) and with ESRAD (black). Here we can see that the model results, although agreeing in general tendencies, lack much of the detail of the

real atmosphere. In particular, the radiosonde and radar measurements show much more structure in the profiles of wind speed, implying stronger wind-shears, compared to the model. Further, the WRF winds underestimate upper-troposphere wind maxima (14:00 UTC on 23 January , 12:00 and 14:00 UTC on 24 January). The WRF estimates of ω_B show a very smooth transition in stability from the lower troposphere to the stratosphere, in contrast to the sharp tropopause transition in the observations. The narrow regions where ω_B is close to zero in the radiosonde measurements, at 14:00 UTC on 23 January, are not represented in the model. On the other hand, a narrow zone with ω_B close to zero is found in the model at 19:00 UTC on 24 January, but is not seen by the radiosonde (although the radiosonde sees ω_B close to zero a little higher up).

The 4th panel of Fig. 5 shows the vertical wind. The model reproduces both the amplitudes and the rapid changes in direction seen in the observations rather well. On 23 and 24 January there is good agreement between model and observations in vertical wavelength, amplitude and direction of the perturbations in the vertical wind. On 25 January, the amplitudes agree well, but the vertical wavelength differs so that the signs of the perturbations in the model are opposite in the upper troposphere, compared to the lower troposphere, whereas the observations show the same sign at all heights. The observed vertical winds are rather more variable in time than the modelled winds, which can give the impression that the observed amplitudes are less. This comparison is considered in more detail below.

Figure 7 shows plan-views of the waves in the vertical wind, for 3 selected times, for the model level lying at 3000 m height above Esrange. The first example, at 00:00 UTC on 24 January, corresponds to surface wind from the southwest, the second to wind from the south-southwest, and the third to wind from the northwest. It is clear that the alignment of the wave fronts and the horizontal wavelength of the dominating waves varies with the wind direction. It is also clear that the amplitudes are highest when the wind is from the northwest, i.e. perpendicular to the mountain chain. Wavelengths vary between about 10 km, and about 20 km. In the first example, the longer wavelength dominates but a localised wave train with the smaller wavelength can be seen close

ACPD
9, 20775–20817, 2009

to the ESRAD location. It is clear that the direction of the vertical wind at the ESRAD site will be very sensitive to the exact position of these waves. Given the temporal and spatial limitations of the meteorological data input to the model, it is not surprising that there is no exact match in the timing of changes in vertical wind directions, between the model and ESRAD.

Figure 8 illustrates the sensitivity of the vertical wind to model parameters. Model runs with only the coarse-resolution, 15 km, grid give vertical wind perturbations an order of magnitude less than those observed by the radar. Using the 3 km grid, the amplitudes of the vertical wind perturbations approach those observed, but the variability in time is much less, and there is rarely agreement in the sign. With the 1 km grid (either 350 m or 150 m vertical resolution) both the amplitude and the temporal variability in the vertical wind are reasonably well represented by the model. Over many intervals, there is also agreement in sign. The sensitivity to the horizontal resolution applies irrespective of height resolution, or of the model top-height used, although the exact details of the temporal variability are closest to the observations when the highest vertical resolution (150 m) is used.

The lowest panel of Fig. 5 shows the bulk Richardson number, R_i . Values less than 1 are generally considered necessary to sustain wind-shear driven turbulence, less than 0.25 to initiate shear-driven turbulence. The model predicts such conditions in the boundary layer, below ~1200 m height, almost all of the time. However, ESRAD is not able to make measurements at such low heights. Short periods with R_i<1 are also predicted in the lower troposphere on the afternoon of 23 January, the afternoon of 24 January and the morning of 25 January. Values approaching this threshold are predicted in the upper troposphere on the afternoon of 25 January. The model also predicts a very short period of convective instability (R_i<0) at about 18:00 UTC on 24 January (at 3000–5000 m height). Clearly there is only a loose correlation between the model and the radar observations concerning the occurrence of turbulence.

Figure 9 illustrates the sensitivity of the model results for R_i to the model parameters and compares in more detail with the ESRAD observations. The model predictions of

regions of lower-tropospheric turbulence (above the boundary layer), are not particularly sensitive to the horizontal resolution but are very sensitive to the height resolution used. Intervals when turbulence could be sustained (R_i<1) and of shear-driven instability (R_i<0.25) are occasionally predicted by the model, for any horizontal resolutions (15, 3 or 1 km, only 15 and 1 km are shown in Fig. 9) so long as the height resolution is 350 m or less. The depth of the minima in R_i are deepest (as low as zero) when the finest height resolution (150 m) is used. However, occurrences of convective instability, R_i<0, are seen only when 1 km horizontal resolution is used for the model. The intervals of low R_i, at around 00:00 UTC on 24 January, 18:00–19:00 UTC on 24 January, to a lesser extent at 04:00–06:00 UTC on 25 January, are much shorter than the duration of the V_{RMS} enhancement observed by ESRAD. Also, the peaks in V_{RMS} do not appear at exactly the times of lowest R_i.

The situation at 19:00 UTC on 24 January , where the model predicts convective instability at about 5000 m height, can be seen in more detail in Fig. 4. It can be seen that the radiosonde does not detect such low buoyancy frequency as the model predicts, in agreement with the lack of turbulence detected by the radar at that height. Figure 10 examines in more detail the differences between the model results and ESRAD observations at 2 further times. At 00:00 UTC on 24 January, the model predicts a wind minimum at 4000 m height, with strong shears above and below, which lead to low values of R_i. There is no wind minimum in the ESRAD observations at this time and no turbulence at 4000 m height. The opposite applies at 06:00 UTC on 25 January, when ESRAD detects a wind minimum, shears and turbulence, while the model does not predict this. Clearly small differences like this can explain a lack of exact match between model predictions for low R_i and observed turbulence.

To further understand the reasons for the turbulence and the differences between the observations and the model, it is instructive to consider the synoptic cross sections in Fig. 11. These are latitude-height sections, at the longitude of the radar, for the outermost model domain with 15 km horizontal resolution. The figure illustrates how, in both cases shown, the tropopause height (roughly the red-yellow boundary) decreases

from south to north. Below the tropopause, a deep air mass starting in the south, with relatively high static stability, overlies a shallower airmass from the north, with relatively low static stability. The wind speed increases sharply in height at about the location of the sloping boundary between the two air masses. (Both examples can be recognised as tropopause folds as described in Rao and Kirkwood, 2005, although this is clearest for the example for 24 January). A combination of high windshear and low stability favours turbulence. Above the lee of the mountains (68°–69° N) both the static stability and the wind speed show wave-like variations in height. These are signatures of long-wavelength inertial gravity waves which can lead to combinations of low stability and high wind shear at slightly different latitudes and heights depending on the exact location of these waves. Inertial gravity waves for this time period, with horizontal wavelengths of 100 s of km, and vertical wavelengths of a few km, have been modelled by Serafimovich et al. (2006), who found that both orographic effects and the upper-troposphere wind jet contributed to generating the waves. In reality, further perturbations will be added to those inertial waves i.e. from the waves with 10–20 km horizontal wavelength, which are not present in the model results at 15 km horizontal resolution. These high-amplitude small-scale waves can result in localised reduction of the static stability in parts of the wave field. This is illustrated by Fig. 12, which shows E–W cross-sections for the high-resolution domain, through ESRAD. Thin wave-induced layers of convective instability, i.e. $\omega_B<0$ (enclosed by the white contour), can be seen in parts of the wave field.

Figure 13 considers average occurrence rates for turbulence (from ESRAD) and for conditions supporting turbulence (from WRF at the ESRAD location). Figure 13a, b show averages over the whole 3-day case study period. Enhanced turbulence levels are rather more common than intervals of $R_i<1$, with turbulence occurrence rates closer to those for $R_i<2$. In the lower troposphere, the height profiles of $V_{RMS}>0.3$ m/s and of $R_i<2$ are similar. Peak occurrence rates of both conditions have values 0.4–0.6 between 2000 m and 3000 m heights and fall off in similar ways towards the upper troposphere. In the upper troposphere the occurrence rates of both $V_{RMS}>2$ m/s and of

ACPD
9, 20775–20817, 2009

R_i<2 are very low. Considering that thin layers with low ω_B, or higher wind shear, are more common in the radiosonde profiles than in the model, it seems likely that regions of low R_i in the lower troposphere are simply not resolved by the model resolution, so their occurrence rate is underestimated.

It is interesting to note that a similar result has been found in a parallel comparison of WRF model results with radar observations of turbulence in mountain wave conditions in Antarctica (Valkonen et al., 2009). In the latter study, the radar was situated on a small isolated nunatak with the mountain wave forming directly overhead. Turbulent layers were detected by the radar between 2000 m and 6000 m height, corresponding reasonably well to regions where the WRF model simulated a lowering of Richardson number to values between 0.5 and 2.

6 Discussion

The model results tell us that the turbulence we observe in the lower troposphere occurs in the same conditions as mountain-waves. However, while the dominant mountain waves in the model, with 10–20 km horizontal wavelength are most sensitive to the horizontal resolution used, the conditions for turbulence are most sensitive to the vertical resolution. This suggests that the mountain waves are not the direct cause of the turbulence at the radar site. This is further supported by Fig. 14, which shows occurrence rates for various conditions over the whole area covered by the intermediate model domain. The region where R_i<2 is common, i.e. likely turbulence, is very different from the region where high vertical winds are common, i.e. high-amplitude mountain waves. As we have seen in the sections above, in the lower troposphere, turbulence is primarily due to strong wind shears, localised in height, but extended horizontally over large parts of the model domain. These are associated with wind shear at upper-level fronts which separate relatively stable air from the south from relatively unstable air from the north. Although this is the main underlying cause of conditions supporting turbulence, perturbations due to the mountain waves can act to further de-

ACPD
9, 20775–20817, 2009

crease R_i , particularly by reducing ω_B in some parts of the waves, as can be seen in Fig. 12.

The WRF model runs which we have made do not include all possible aspects of cloud-related turbulence. For example, cloud-top radiative cooling (see e.g. Vihma et al., 2005) is a possible source of turbulence which is likely not captured accurately by our WRF simulations. Records of the cloud cover during our case study exist in the form of all-sky photographs during the night hours, from a camera located 20 km east of the radar site which monitors the aurora (http://www.irf.se/allsky/), and in the records of lidar observations from the same site as the radar (K. H. Fricke, personal communication, 2003, Blum et al., 2006). Both of these sources showed that there were clear skies during most of the time, between 19:00–04:00 UTC on the night 23/24 January and between 23:00–06:00 UTC on 24/25 January. The turbulent layers in the lower troposphere were seen by the radar throughout those periods, so the turbulence cannot have been due to cloud-induced effects.

The model itself does not completely explain the observed occurrence of turbulence if we consider that the bulk Richardson number should be less than 1 to support turbulence. However, there is reasonable agreement in height and time between model predictions of reasonably low Richardson number (R_i<2) and the observed occurrence of turbulence. A full description of the statistics of mountain wave conditions from the ESRAD radar is beyond the scope of the present paper, but it can be mentioned that mountain-wave/ turbulence conditions as in our case study have occurred about 40% of the time in the whole database from 1996 to the present. So turbulence in the lower troposphere is common.

To be able to estimate the effect of this turbulence in terms of vertical mixing of the atmosphere, we need to be able to estimate the rate at which turbulent energy (which is measured directly by V^2_{RMS}) is converted to vertical mixing or eddy diffusivity (which implies an increase in potential energy). The physics of turbulent mixing in a stably-stratified atmosphere has been addressed by Weinstock (1978), leading to an

ACPD
9, 20775–20817, 2009

expression for vertical eddy diffusivity K

$$K \sim 0.4 V_{\mathrm{RMS}}^2 / \omega_B \tag{3}$$

(Note that the value of the numerical constant in this expression varies between different derivations. The value here, 0.4, is among the highest found in the literature, while Kurosaki et al., 1996, for example, use one of the lowest values, 0.1). The characteristic time for vertical mixing (for example the relaxation of the vertical gradient in ozone mixing ratio, assuming no new sources), is given by (e.g. Goody, 1995)

$$t_K \sim H^2 / K \tag{4}$$

where H is the density scale height, which is ~7 km. In terms of measured V_{RMS}, this gives

$$t_K \sim 2.5 \omega_B H^2 / V_{\mathrm{RMS}}^2 \tag{5}$$

Clearly, t_K will be very sensitive to the buoyancy frequency ω_B. The mean value of ω_B in the conditions of R_i<2 at the location of ESRAD (for the WRF results shown in Fig. 5) is $10^{-2}\mathrm{s}^{-1}$. For the rather high value of V_{RMS}=1 m/s, this would lead to t_K ~14 days, which would imply a rather slow rate of mixing. On the other hand, t_K will be reduced to zero in conditions of convective instability ($\omega_B \leq 0$). The theoretical considerations of Weinstock (1978) do not really apply in these conditions. However, 3-D turbulence simulations of breaking waves (which is essentially the conditions which here would correspond to ω_B falling to zero) have shown that mixing is indeed very rapid, with time scale of the order of a buoyancy period (Fritts et al., 2003).

The possibility that air masses flowing across the mountains might encounter regions of convective instability, is very important for the possibility of rapid vertical mixing. Figure 15 shows the occurrence rate of low Richardson numbers averaged over the whole inner model domain, and, on the right hand side, the chance that an air mass will encounter convective instability. The domain-averaged occurrence rates of low

Richardson number are much like those for the ESRAD site alone (Fig. 13), however when considered in terms of the chance of convective mixing anywhere along the path, the rates are much higher, 5–10%. Since the time spent by an air mass in crossing such a region (Fig. 12) will be of the order of a buoyancy period, the air within the layer affected can be completely mixed. Although mixing at any particular place and time is likely to be confined to a thin layer, the air column is likely to encounter further mixing layers at slightly different heights as it flows across the mountains.

As we have seen in the radiosonde comparison, the model seems to underestimate the occurrence of thin layers of very low ω_B so that the 5–10% chance of convective mixing in Fig. 15 may be an underestimate. However, the uncertainty in this is too large to allow us to make direct quantitative predictions of vertical mixing on the basis of the model results, or the radar measurements alone.

7 Conclusions

Comparison between radar observations and the WRF model show that mountain waves with small horizontal wavelength (10–20 km) and up to a few m/s vertical velocities dominate the behaviour of the vertical wind field over northern Scandinavia. These waves are represented in the model only when it is run with a horizontal resolution of 3 km or better. In the lower troposphere, periods of enhanced turbulence are seen by the radar at the same time as the mountain waves. Comparison with the WRF model results show that the main reason for the turbulence is wind-shears at upper-level synoptic fronts. However, the added effects of small-horizontal-scale mountain waves can lead to an increase in the occurrence rate of conditions likely to lead to turbulence, including localized increases in wind shear and occasional lowering of the buoyancy frequency to below zero. The occurrence rate of turbulence as seen by the radar corresponds reasonably well with the occurrence rate of conditions with Richardson number <2 in the model, both in overall amount and in the height profile.

Radar observations over a longer time can reasonably be used to make a qualitative

assessment of the occurrence of turbulent mixing in the lower troposphere, its variations over time on different scales (hours to seasonal), over height, and its relation both to synoptic systems and to mountain waves. There is a large uncertainty, and possibly a large scatter, in the buoyancy frequency within the narrow layers where turbulent mixing most likely takes place. This makes it difficult to make quantitative estimates of the overall time scale of vertical mixing in the air-flow over the region, using only the radar observations or the WRF model results.

Comparison of height profiles of a suitable tracer, such as ozone in wintertime, at different points along the path of airflow across the mountains, would be a possible method to examine this problem further.

Acknowledgements. The ESRAD radar is jointly owned and operated by Swedish Institute of Space Physics and Swedish Space Corporation. This research has been made possible by grants from Swedish Research Council, Swedish Development Agency and the Kempe foundation. WRF was developed at the National Center for Atmospheric Research (NCAR) which is operated by the University Corporation for Atmospheric Research (UCAR). Cloud images (from NOAA GOES satellite) are archived and provided by the NERC Dundee satellite Center. Meteorological data from the NCEP Global Forecasting system data were provided by the Data Support Section of the Computational and Information Systems Laboratory at the National Center for Atmospheric Research. NCAR is supported by grants from the National Science Foundation. We thank R. Goldberg and F. Schmidlin, NASA, for providing radiosonde data which were part of the MaCWAVE sounding rocket campaign.

References

Blum, U., Baumgarten, G., Schoech, A., Kirkwood, S., Naujokat, B., and Fricke, K. H.: The atmospheric background situation in northern Scandinavia during January/February 2003 in the context of the MaCWAVE campaign, Ann. Geophys., 24, 1189–1197, 2006, http://www.ann-geophys.net/24/1189/2006/. 20780, 20793

Briggs, B. H.: The analysis of spaced sensor records by correlation techniques, in: Handbook for MAP, 13, 166–186, Univ. of Ill., Urbana, 1984. 20782

Chilson, P., Kirkwood, S., and Nilsson, A.: The Esrange MST radar: A brief introduction and procedure for range validation using balloons, Radio Sci., 34, 427–436, 1999. 20778, 20781
Cohn, A.: radar measurements of turbulent eddy dissipation rate in the troposphere : a comparison of techniques, J. Atmos. Ocean. Tech., 12, 85–95, 1995. 20785
Dibb, J., Talbot, R., Scheuer, E., Seid, G., DeBell, L., Lefer, B., and Ridley, B.: Stratospheric influence on the northern North American free troposphere during TOPSE: 7Be as a stratospheric tracer, J. Geophys. Res., 108, 8863, doi:10.1029/2001JD001347, 2003. 20777
Dörnbrack, A.: Turbulent mixing by breaking gravity waves, J. Fluid Mech., 375, 113–141, 1998. 20777
Dörnbrack, A., Birner, T., Fix, A., Flentje, H., Meister, A., Schmid, H., Bromwell, E., and Mahoney, M.: Evidence for intertia gravity waves forming polar stratospheric clouds over Scandinavia,, J. Geophys. Res., 107, 8287, doi:10.1029/2001JD000452, 2002. 20778
Doyle, J. D. and Durran, D. R.: Recent developments in the theory of atmospheric rotors, B. Am. Meteorol. Soc., 85, 337–342, doi:10.1175/BAMS-85-3-337, 2004. 20777
Doyle, J. D. and Durran, D. R.:The dynamics of mountain-wave induced rotors, J. Atmos. Sci., 59, 186–201, 2002. 20777
Doyle, J., Shapiro, M., Jiang, Q., and Bartels, D.: Large-amplitude mountain wave breaking over Greenland, J. Atmos. Sci., 62, 3106–3126, 2005. 20779
Dudhia, J.: Numerical study of convection observed during the winter monsoon experiment using a mesoscale two-dimensional model, J. Atmos. Sci, 46, 3077–3107, 1989. 20787
Fritts, D. C., Bizon, C., Werne, J. A., and Meyer, C. K.: Layering accompanying turbulence generation due to shear instability and gravity wave breaking, J. Geophys. Res, 108, 8452, doi:10.1029/2002JD002406, 2003. 20794
Fukao, S., Yamanaka, M. D., Ao, N., Hocking, W. K., Sato, T., Yamamoto, M., Nakamura, T., Tsuda, T., and Kato, S.: Seasonal variability of vertical eddy diffusivity in the middle atmosphere 1. Three-year observations by the middle and upper atmosphere radar, J. Geophys. Res., 99, 18973–18987, 1994. 20778
Gage, K.: Radar observations of the free atmosphere : structure and dynamics, in: Radar in Meteorology, edited by: Atlas, D., American Meteorological Society, Boston, 1990. 20782, 20785
Goldberg, R. A., Fritts, D. C., Schmidlin, F. J., Williams, B. P., Croskey, C. L., Mitchell, J. D., Friedrich, M., Russell III, J. M., Blum, U., and Fricke, K. H.: The MaCWAVE program to study gravity wave influences on the polar mesosphere, Ann. Geophys., 24, 1159–1173, 2006,

http://www.ann-geophys.net/24/1159/2006/. 20780, 20781
Goody, R.: Principles of atmospheric chemistry and physics, Oxford University Press, New York, 1995. 20794
Hoffmann, P., Serafimovich, A., Peters, D., Dalin, P., Goldberg, R., and Latteck, R.: Inertia gravity waves in the upper troposphere during the MaCWAVE winter campaign – Part I: Observations with collocated radars, Ann. Geophys., 24, 2851–2862, 2006, http://www.ann-geophys.net/24/2851/2006/. 20780
Holdsworth, D. A., Vincent, R. A., and Reid, I. M.: Mesospheric turbulent velocity estimation using the Buckland Park MF radar, Ann. Geophys., 19, 1007–1017, 2001, http://www.ann-geophys.net/19/1007/2001/. 20782, 20785
Holdsworth, D. A. and Reid, I. M.: Comparisons of full correlation analysis (FCA) and imaging Doppler interferometry (IDI) winds using the Buckland Park MF radar, Ann. Geophys., 22, 3829–3842, 2004, http://www.ann-geophys.net/22/3829/2004/. 20782
Hong, S.-Y., J. D. and Chen, S.-H.: A revised approach to ice microphysical processes for the bulk parameterization of clouds and precipitation, Mon. Weather Rev., 132, 103–120, 2004. 20787
Hooper, D. A., Arvelius, J., and Stebel, K.: Retrieval of atmospheric static stability from MST radar return signal power, Ann. Geophys., 22, 3781–3788, 2004, http://www.ann-geophys.net/22/3781/2004/. 20782
James, P., Stohl, A., Forster, C., Eckhardt, S., Seibert, P., and Frank, A.: A 15-year climatology of stratosphere-troposphere exchange with a Lagrangian dispersion model 2. Mean climate and seasonal variability, J. Geophys. Res., 108, 8522, doi:10.1029/2002JD002639, 2003. 20777
Kurosaki, S., Yamanaka, M. D., Hashiguchi, H., Sato, T., and Fukao, S.: Vertical eddy diffusivity in the lower and middle atmosphere: A climatology based on the MU radar observations during 1986–1992, 58, 727–734, 1996. 20778
Larsson, L.: Observations of lee wave clouds in the Jämtland Mountains, Sweden, Tellus, 6, 124–138, 1954. 20776
Luce, H., Hassenpflug, G., Yamamoto, M., and Fukao, S.: Comparisons of refractive index gradient and stability profiles measured by balloons and the MU radar at a high vertical resolution in the lower stratosphere, Ann. Geophys., 25, 47–57, 2007, http://www.ann-geophys.net/25/47/2007/. 20782

Maturilli, M. and Dörnbrack, A.: Polar stratospheric ice cloud above Spitsbergen, J. Geophys. Res., 111, doi:10.1029/2005JD006967, 2006. 20779

Mlawer, E., Taubman, S., Brown, P., Iacono, M., and Clough, S.: Radiative transfer for inhomogeneous atmospheres: RRTM, a validated correlated-k model for the longwave, J. Geophys. Res., 102, 16663–16682, 1997. 20787

Nastrom, G. D., Gage, K. S., and Ecklund, W. L.: Variability of Turbulence, 4–20 km, in Colorado and Alaska From MST Radar Observations, J. Geophys. Res., 91, 6722–6734, 1986. 20778

Nastrom, G. and Eaton, F.: Turbulence eddy dissipation rates from radar observations at 5–20 km at White Sands Missile Range, New Mexico, 102, 19495–19505, 1997. 20778

Nastrom, G. D. and Eaton, F. D.: Seasonal variability of turbulence parameters at 2 to 21 km from MST radar measurements at Vandenberg Air Force Base, California, 110, 19495–19505, 2005. 20778

Pluogonven, R., Hertzog, A., and Teitelbaum, H.: Observations and simulations of a large-amplitude mountain wave breaking over the Antarctic Peninsula, J. Geophys. Res., 113, D16113, doi:10.1029/2007JD009739, 2008. 20779, 20780

Rao, D. N., Rao, T. N., Venkataratnam, M., Thulasiraman, S., Rao, S. V. B., Srinivasulu, P., and Rao, P. B.: Diurnal and seasonal variability of turbulence parameters observed with Indian mesosphere-stratosphere-troposphere radar, Radio Sci., 36, 1439–1457, 2001. 20778

Rao, T. and Kirkwood, S.: Characteristics of tropopause folds over Arctic latitudes, J. Geophys. Res., 110, D18102, doi:10.1029/2004JD005374, 2005. 20777, 20791

Rao, T., Kirkwood, S., Arvelius, J., von der Gathen, P., and Kivi, R.: Climatology of UTLS ozone and the ratio of ozone and potential vorticity over northern Europe, J. Geophys. Res., 108, 4703–4711, doi:10.1029/2003JD003860, 2003. 20777

Rao, T. N., Arvelius, J., and Kirkwood, S.: Climatology of tropopause folds over a European Arctic station (Esrange), J. Geophys. Res., 113, D00B03, doi:10.1029/2007JD009638, 2008. 20777

Réchou, A., Barabash, V., Chilson, P., Kirkwood, S., Savitskaya, T., and Stebel, K.: Mountain wave motions determined by the Esrange MST radar, Ann. Geophys., 17, 957–970, 1999, http://www.ann-geophys.net/17/957/1999/. 20778

Serafimovich, A., Zülicke, Ch., Hoffmann, P., Peters, D., Dalin, P., and Singer, W.: Inertia gravity waves in the upper troposphere during the MaCWAVE winter campaign – Part II: Radar investigations and modelling studies, Ann. Geophys., 24, 2863–2875, 2006, http://www.ann-geophys.net/24/2863/2006/. 20778, 20780, 20791

Skamarock, W., Klemp, J., Dudhia, J., Gill, D., Barker, D., Wang, W., and Powers, J.: A description of the Advanced research WRF version 2,, NCAR Tech. Note NACR/TN-468+STR, National center for Atmospheric Research, Boulder, Colorado, 2005, revised, 2007. 20780, 20786, 20787

Sprenger, M. and Wernli, H.: A northern hemisphere climatology of cross-tropopause exchange for the ERA15 time period (1979–1993), J. Geophys. Res., 108, 8251, doi:10.1029/2002JD002636., 2003. 20777

Stohl, A.: Characteristics of atmospheric transport into the Arctic troposphere, J. Geophys. Res., 111, D11306, doi:10.1029/2005JD006888, 2006. 20777

Stohl, A., Forster, C., Frank, A., Seibert, P., and Wotawa, G.: Technical note: The Lagrangian particle dispersion model FLEXPART version 6.2, Atmos. Chem. Phys., 5, 2461–2474, 2005, http://www.atmos-chem-phys.net/5/2461/2005/. 20777

Tarasova, O. A., Brenninkmeijer, C. A. M., Jckel, P., Zvyagintsev, A. M., and Kuznetsov, G. I.: A climatology of surface ozone in the extra tropics: cluster analysis of observations and model results, Atmos. Chem. Phys., 7, 6099–6117, 2007, http://www.atmos-chem-phys.net/7/6099/2007/. 20777

Valkonen, T., Vihma, T., Kirkwood, S., and Johansson, M.: Fine-scale model simulation of gravity waves generated by Basen nunatak in Antarctica, Tellus, submitted, 2009. 20792

Vihma, T., Lüpkes, C., Hartmann, J., and Savijärvi, H.: Observations and modelling of cold-air advection over Arctic sea-ice, Bound.-Lay. Meteorol., 117, 275–300, doi:10.1007/s10546-004-6005-0, 2005. 20793

Wang, L., Fritts, D. C., Williams, B. P., Goldberg, R. A., Schmidlin, F. J., and Blum, U.: Gravity waves in the middle atmosphere during the MaCWAVE winter campaign: evidence of mountain wave critical level encounters, Ann. Geophys., 24, 1209–1226, 2006, http://www.ann-geophys.net/24/1209/2006/. 20780

Weinstock, J.: Vertical turbulent diffusion in a stably stratified fluid, J. Atmos. Sci., 35, 1022–1027, 1978. 20793, 20794

Zeng, G., Pyle, J. A., and Young, P. J.: Impact of climate change on tropospheric ozone and its global budgets, Atmos. Chem. Phys., 8, 369–387, 2008, http://www.atmos-chem-phys.net/8/369/2008/.

20777

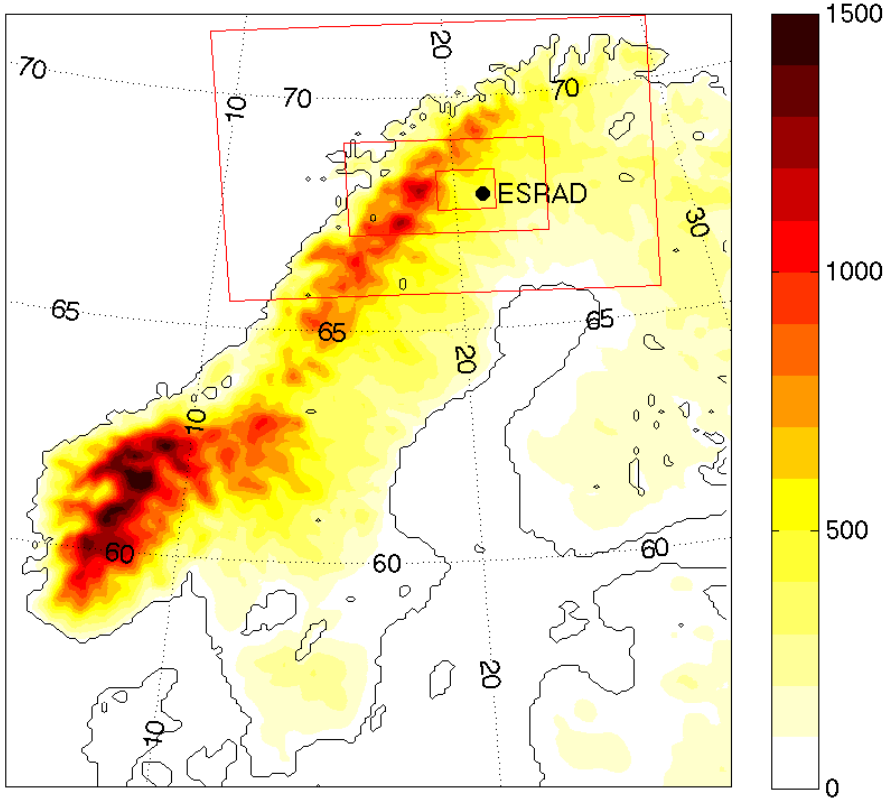

Fig. 1. Map of Scandinavia showing the topography (colour scale with heights in m), the location of the ESRAD radar, and the nested model domains used for the WRF simulations (red rectangles). The outermost domain has horizontal resolution 15 km, the indermediate domain 3 km, and the inner domain around the location of ESRAD has 1 km resolution. Lines of latitude and longitude are shown with dotted lines.

ACPD
9, 20775–20817, 2009

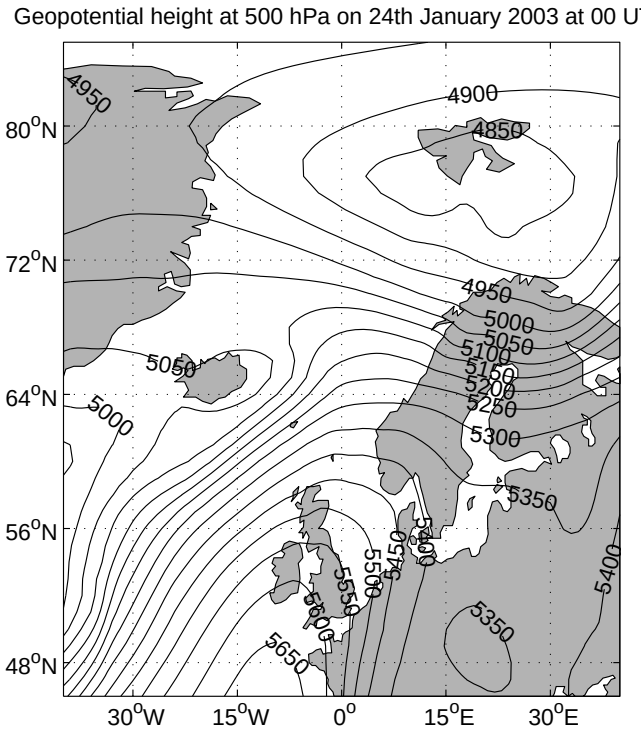

Fig. 2a. Synoptic chart for 00:00 UTC on 24 January 2003: Geopotential height at 500 hPa.

ACPD

9, 20775–20817, 2009

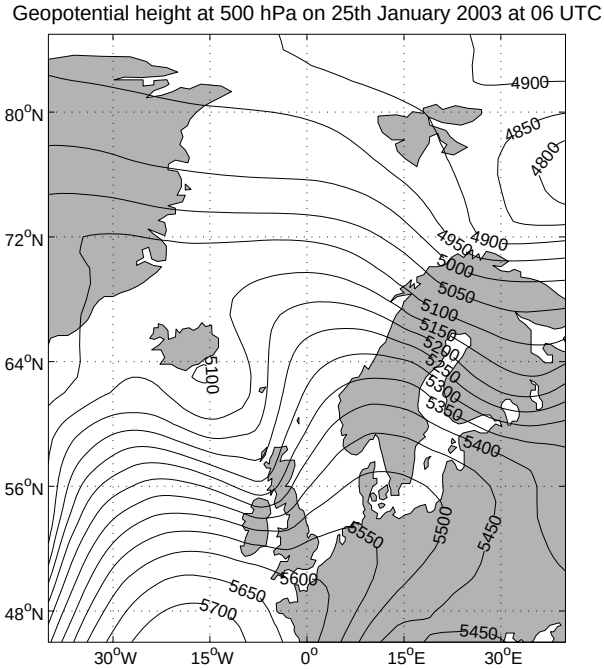

Fig. 2b. Synoptic chart for 06:00 UT on 25 January 2003: Geopotential height at 500 hPa.

ACPD
9, 20775–20817, 2009

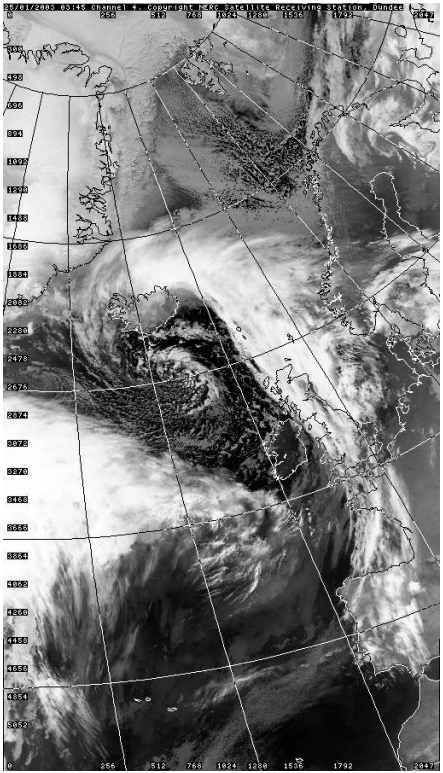

Fig. 3. Satellite cloud image at 03:45 UT on 25 January 2003 (NOAA, IR channel 4 from http://www.sat.dundee.ac.uk).

ACPD

9, 20775–20817, 2009

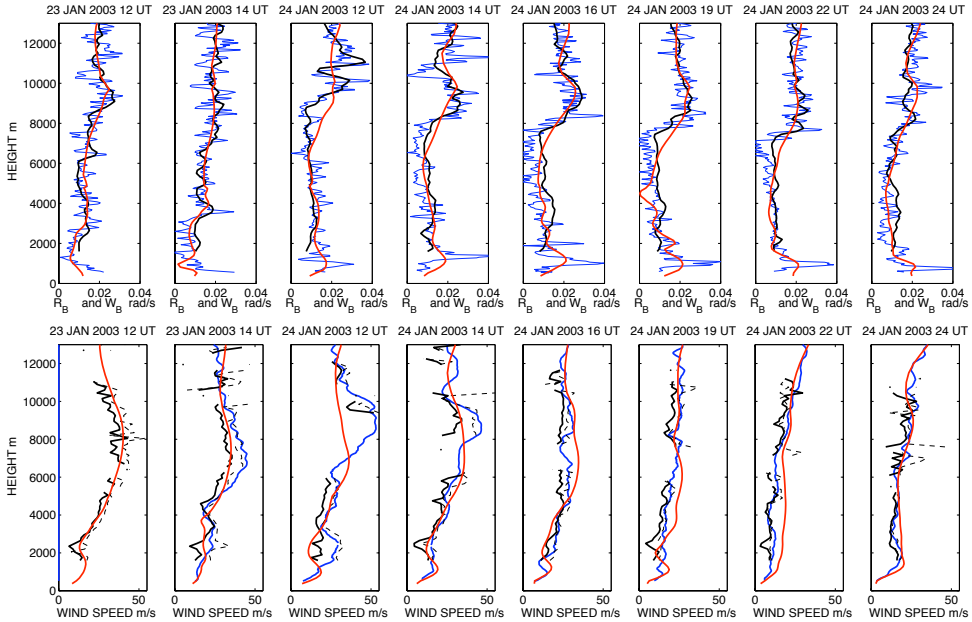

Fig. 4. Radiosonde measurements (blue), ESRAD radar measurements (black) and WRF model results for the ESRAD site (red). All radiosondes were launched from the ESRAD site. ESRAD and WRF results are averaged for 30 min following the launch time. Top row shows buoyancy frequency, lower row wind speed. Solid black lines are f.c.a. true winds, dashed lines are apparent winds. See text for further details.

ACPD
9, 20775–20817, 2009

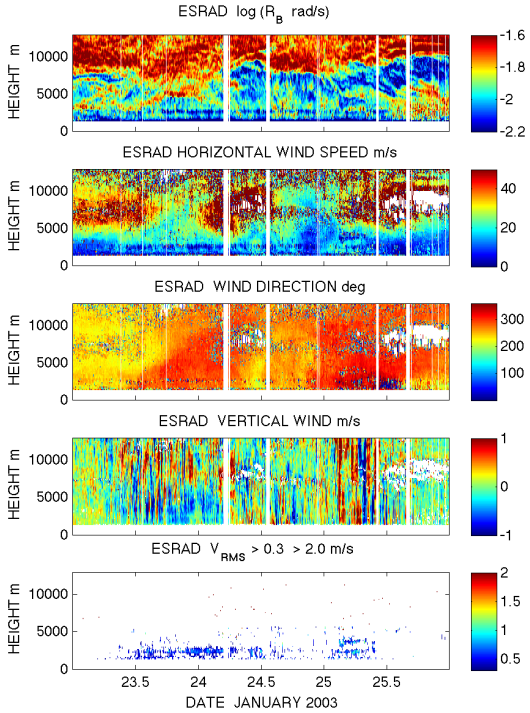

Fig. 5a. Measurements made by the ESRAD radar for 23, 24 and 25 January 2003. Gaps in the data due to interference, or low signal levels (signal-to-noise ratio <0.5) are shown in white. Top panel shows the logarithm of the radar estimate of buoyancy frequency, R_B. next two panels show the speed and direction of the horizontal wind (true wind from f.c.a. analysis). The direction from which the wind is blowing is given in degrees clockwise from north. The 4th panel shows the vertical wind from the Doppler shift of the radar echo (positive upwards). The lowest panel shows turbulent velocities (V_{RMS}). Only values exceeding 0.3 m/s are plotted below 5500 m height, and values above 2 m/s above that height.

ACPD
9, 20775–20817, 2009

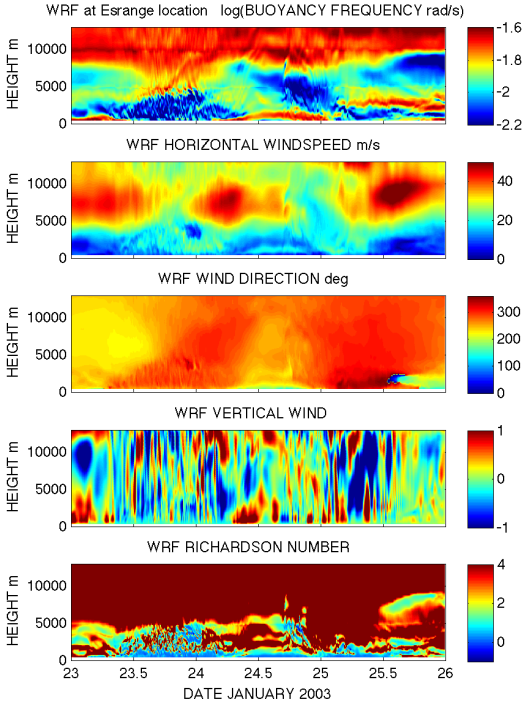

Fig. 5b. Results from the WRF model, for 23, 24 and 25 January 2003, innermost nested domain with 1 km grid spacing, for the location of the ESRAD radar. Top panel shows the logarithm of the buoyancy frequency, ω_B. Next two panels show the speed and direction of the horizontal wind. The direction from which the wind is blowing is given in degrees clockwise from north. The 4th panel shows the vertical wind (positive upwards). The lowest panel shows the bulk Richardson number. See text for further details.

ACPD
9, 20775–20817, 2009

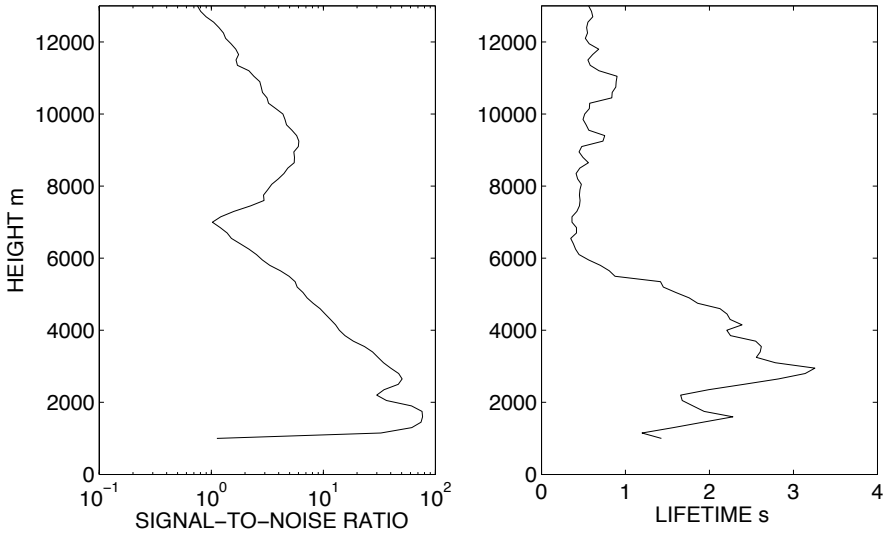

Fig. 6. Vertical profiles of the median values 23–25 January of the radar echo strength (signaltonoise ratio) and diffraction pattern lifetime. See text for further details.

ACPD
9, 20775–20817, 2009

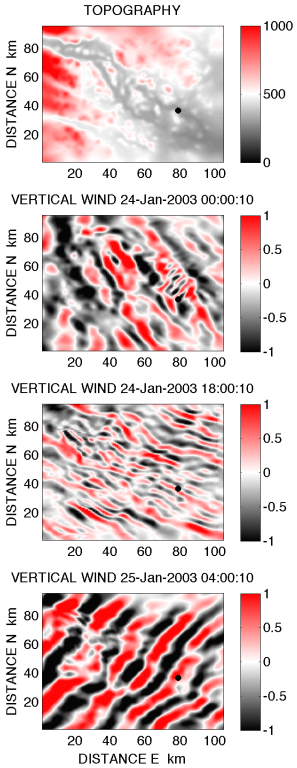

Fig. 7. Plan views of the topography and of the mountain waves, at 3 different times, in the WRF model innermost domain, for the model level which is at 3000 m height above the radar site. Vertical wind is in m/s.

ACPD
9, 20775–20817, 2009

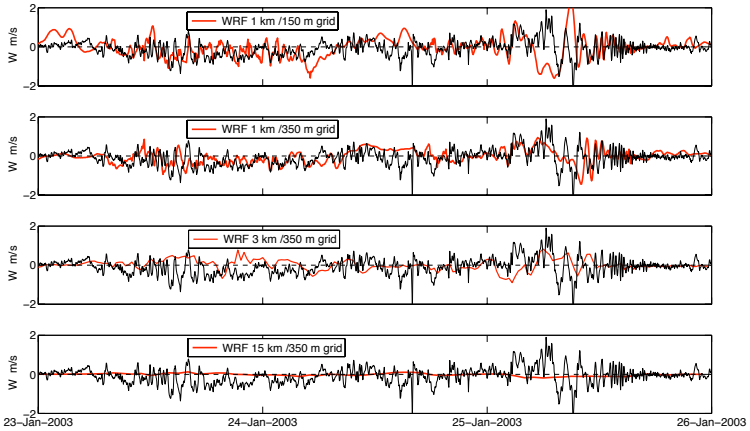

Fig. 8. Comparison between vertical wind velocities measured by ESRAD and WRF model results using different horizontal (1, 3 or 15 km) and vertical (150 or 350 m) resolutions. Measurements and model results at 3000 m height.

ACPD
9, 20775–20817, 2009

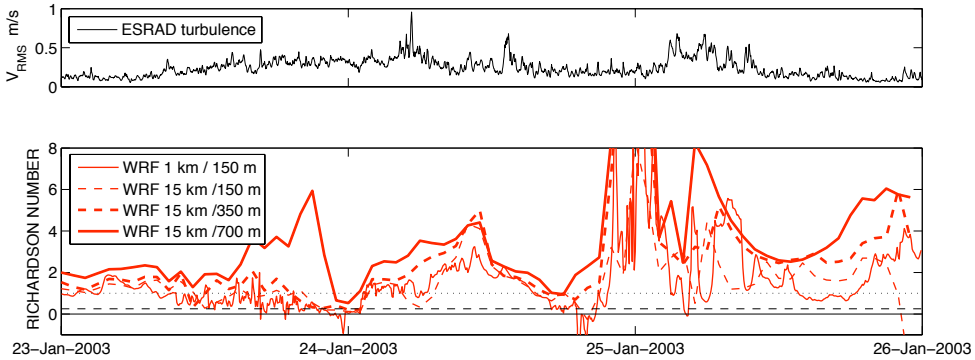

Fig. 9. Comparison between turbulent velocities measured by ESRAD and WRF model estimates of the bulk Richardson number using different horizontal (1 or 15 km) and vertical (150, 350 or 700 m) resolutions. Measurements show the mean V_{RMS} between 2000 and 5000 m heights, model results the minimum Richardson number between the same heights.

ACPD
9, 20775–20817, 2009

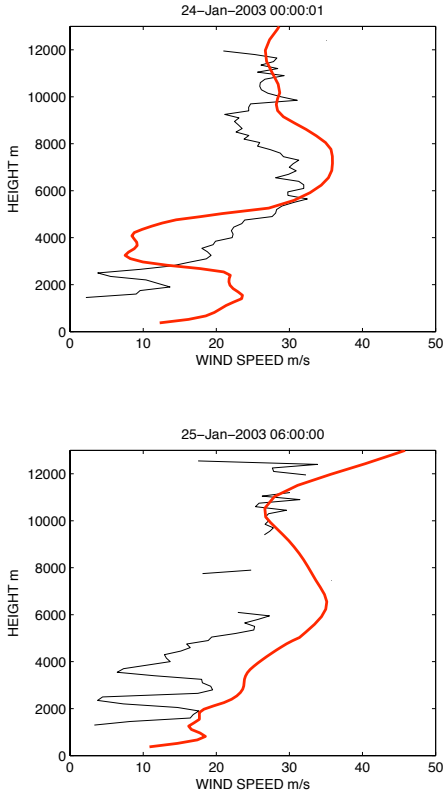

Fig. 10. Comparison of wind profiles between WRF (red) and ESRAD (black). At 00:00 UTC on 24 January and at 06:00 UTC on 25 January.

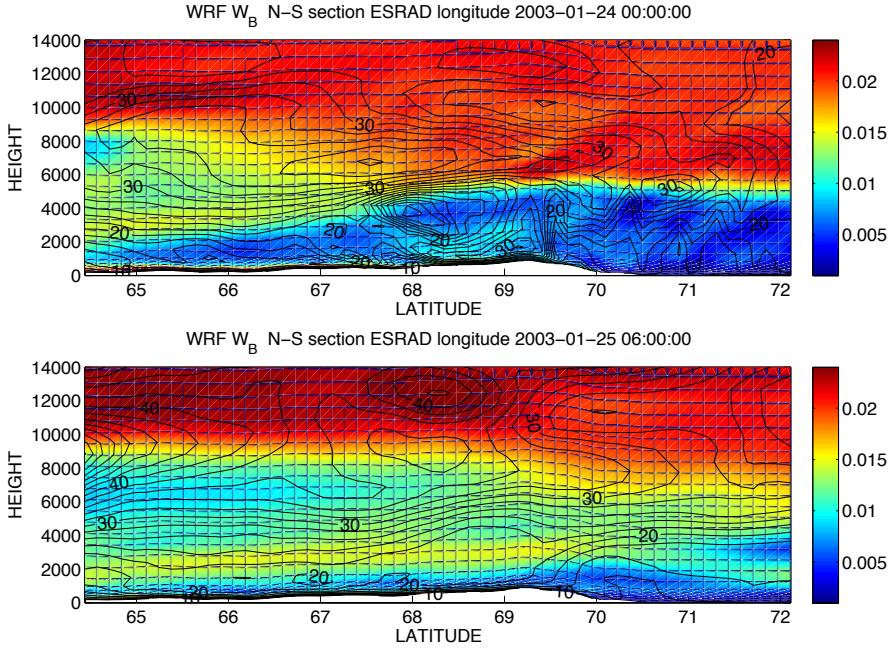

Fig. 11. Latitude-height cross sections of buoyancy frequency (colour scale, units s^{-1}) and wind speed (contours, units m/s) from an extended outermost model domain (15 km horizontal grid). The cross sections are at the ESRAD longitude.

ACPD
9, 20775–20817, 2009

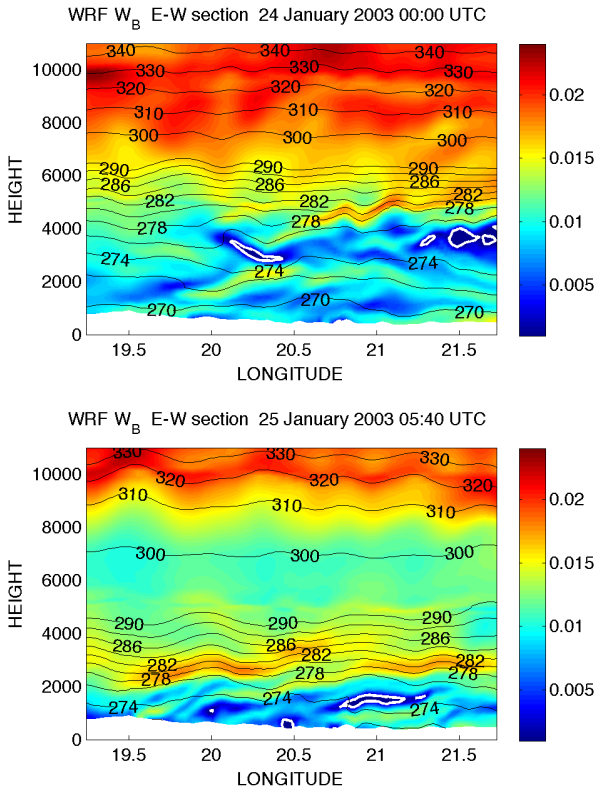

Fig. 12. Longitude-height cross sections of buoyancy frequency (colour scale, units s^{-1}) and potential temperature (black contours, units K). White contours enclose regions of convective instability, i.e. buoyancy frequency <0. From the innermost model domain (1 km horizontal grid) at the ESRAD latitude.

ACPD
9, 20775–20817, 2009

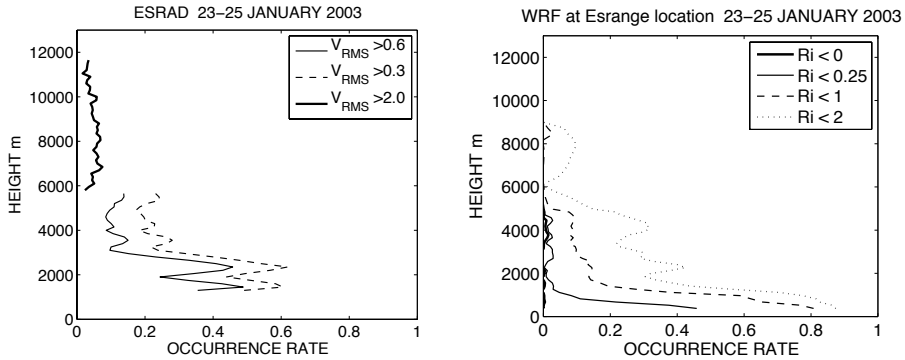

Fig. 13. Occurrence rates of turbulence observed by ESRAD, and low Richardson numbers predicted by WRF for the ESRAD location, for the whole period 23rd–25th January, 2003. WRF results based on 1 km/150 m grid resolution.

ACPD
9, 20775–20817, 2009

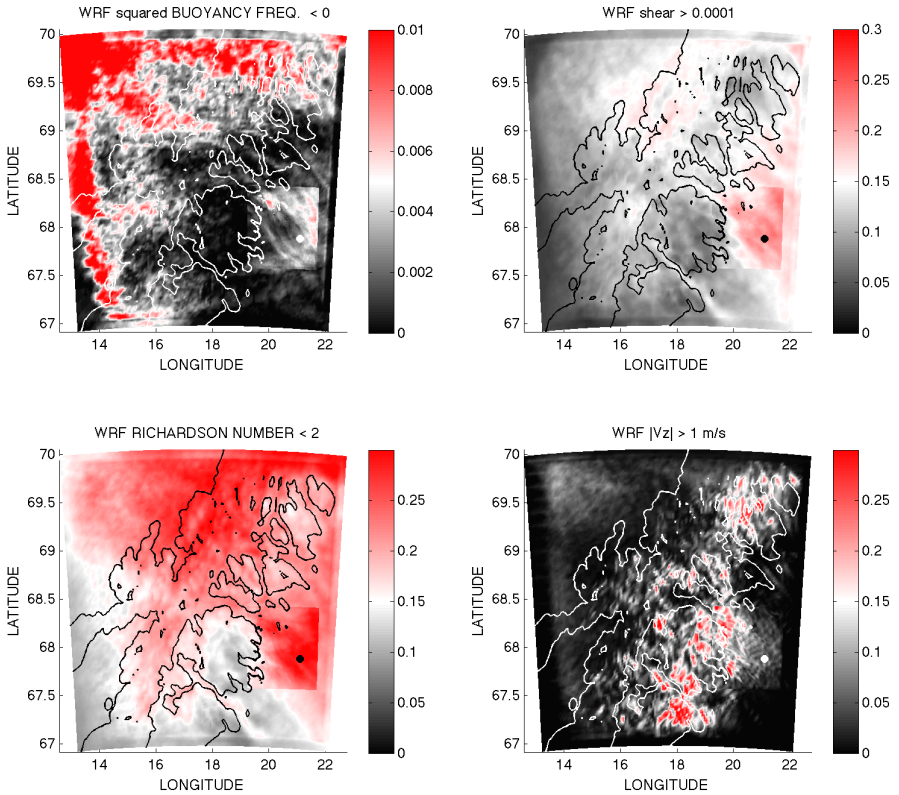

Fig. 14. Plan view of the occurrence rates of ω_B<0, vertical shear in horizontal wind >0.001s^{-1}, Richardson number <2, and vertical wind >1 m/s. Occurrence rates give the average for the period 23–25 January 2003 and for the height interval 2000–5000 m and are plotted first based on WRF simulations for an extended domain with 3 km horizontal and 150 m vertical resolution. Results for the 1 km grid are then superposed.

ACPD
9, 20775–20817, 2009

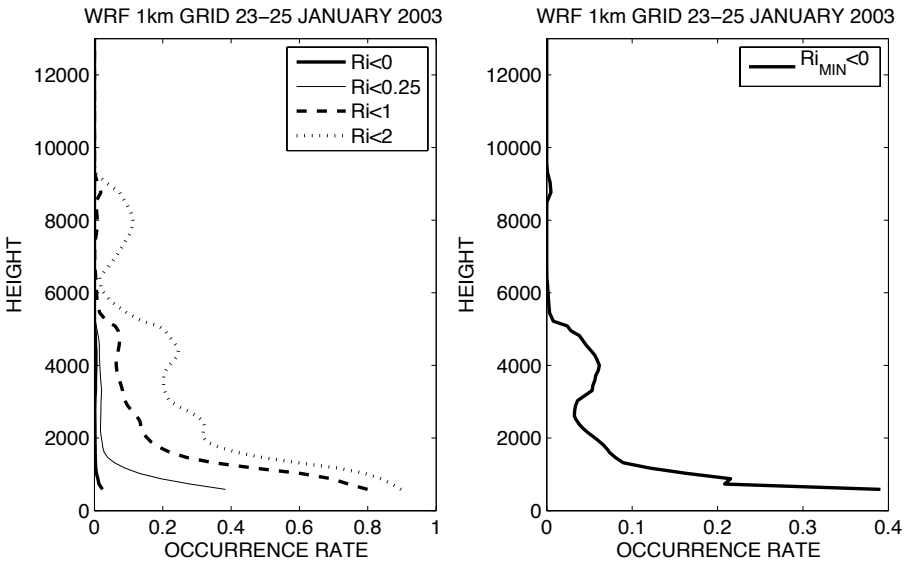

Fig. 15. Left-hand side : occurrence rates for low values of Richardson number for the whole of the innermost model domain, and for the period from 00:00 UTC on 23 January to 24:00 UTC on 25 January 2003. Right-hand side: the average (over latitude and time) of the occurrence rate of convective instability at any location along a latitude circle, within the innermost model domain. This represents the chance that an air-mass crossing the domain will encounter a region of convective instability somewhere along its path from west to east.

ACPD
9, 20775–20817, 2009